Complex behavior in compressible nonisochoric granular flows

James A. Robinson⊙ and Daniel J. Holland⊙*

Chemical and Process Engineering Department, University of Canterbury, 8140 Christchurch, New Zealand

Luke Fullard⊙

School of Fundamental Sciences, Massey University, 4474 Palmerston North, New Zealand

Granular flow models are typically examined within steady isochoric systems where velocity divergence equals zero and properties are uniform along streamlines. Within these flows dilatancy and packing variations can be, and are, neglected. However, there exists a broad range of flows that are nonisochoric, where these variations cannot be ignored. In this paper we examine different nonisochoric systems using discrete element simulations. We first demonstrate that nonisochoric granular flows do not exhibit a simple relationship between stress and packing and that the alignment criterion relating stress to strain rate apply only to well-agitated regions of the flow. Subsequently, the discrete simulation results are used to test the velocity divergence and stress in several compressible granular flow models. We demonstrate that the models are able to capture key features of the nonisochoric flows, though none fully describe the observed behavior. We show that in some cases the predictions of the models can be improved by redefining the equilibrium condition. Finally, we discuss the challenges faced with extending these compressible models into dense regions, where granular flows require nonlocal descriptions of the rheology.

I. INTRODUCTION

A significant challenge when attempting to apply continuum descriptions to granular flows is describing granular packing. Granular materials display dilatancy, expanding, or contracting when sheared, and even in steady incompressible (isochoric) flows packing is not necessarily spatially uniform [1]. Furthermore, many flows of practical interest, such as hoppers, are nonisochoric, with granular packing and other properties varying along streamlines. In this paper we study packing and stress variations in a range of nonisochoric granular flows and examine these in the context of several continuum descriptions of granular flow.

Granular packing and dilatancy can be modeled using discrete element models (DEMs), which model individual particle motion. However, the high computational cost of DEMs means that continuum descriptions of granular flow are desired. Various continuum models have been proposed. Perhaps the most famous of these is the $\mu(I)$ rheology [2], which describes the stress ratio μ as a function of the inertial number I, where I is a dimensionless number that describes the relative importance of shear rate and pressure. The $\mu(I)$ rheology, along with other continuum models developed for dense flows, are applied assuming incompressibility and uniform packing, effectively neglecting to model dilatant effects [2–5]. In some geometries dilatancy has been shown to result in

---

*Corresponding author: daniel.holland@canterbury.ac.nz

the presence of unexpected secondary flows [6,7]. Characterizing compressibility is likely important to fully describe the observed phenomena.

DEM simulations have shown that for dense, steady-state flows packing fraction (ϕ) is well described as a function of the inertial number I [1]. However, in dense, weakly sheared regions of flow this relationship does not hold [8–10]. In these regions where μ drops below the static yield criterion, it is well known that the $\mu(I)$ relationship does not apply. In these dense regions, stress is not locally dependent on I and instead the behavior of neighboring regions of flow must be considered [4,11]. Hence these flows exhibit "nonlocal" behavior [4], including slow creeping flow [12]. Recently it has been shown that for isochoric flows, which are steady in both an Eulerian and Lagrangian sense, ϕ can be described as a local function of μ [8,9], even in regions of flow that exhibit nonlocal behavior. However, for steady, nonisochoric flows, which are transient in a Lagrangian sense, more complex behavior was observed [8].

Steady nonisochoric flows represent a broad category of flow geometries, including rotating drums, flows through pipes or chutes where obstructions are present, hoppers, and others. For isochoric flows velocity divergence ($\nabla \cdot \mathbf{u}$) equals 0 throughout the system and continuum flow properties (such as velocity, pressure and packing) are uniform along streamlines. In nonisochoric systems, $\nabla \cdot \mathbf{u} \neq 0$ and properties vary along streamlines. There has been limited work modeling steady nonisochoric systems. The incompressible $\mu(I)$ model has been applied to some transient nonisochoric systems [2,13–15]. Most notably, this approach could qualitatively, but not quantitatively, reproduce flow profiles in hoppers [16]. Furthermore, in some cases the incompressible $\mu(I)$ model can become ill-posed [17–19], though regularized forms of $\mu(I)$ have been developed which aim to correct for this [17,20].

Several continuum approaches that incorporate some form of dilatancy have been proposed [21–24]. These approaches modify the $\mu(I)$ equation for stress and incorporate an additional equation to describe velocity divergence. In practice, the velocity divergence relationship is often inverted and used to describe pressure. Many of these models are designed to collapse to the standard incompressible $\mu(I)$ response for isochoric flows. Different compressible models have been applied, with some success, to model transient flows down inclined planes and in shear cells [24,25]. However, none of these models has seen broad application or been tested in a wide variety of geometries.

In this work we seek to examine how several existing compressible continuum models reflect the behavior we observe in steady nonisochoric flows. To accomplish this, we use DEM simulations to model three geometries which exhibit nonisochoric flow (hereafter referred to as nonisochoric flow geometries), namely, a pseudo-2D hopper and chutes with different inserts. Using these simulations we examine key aspects of three recent local compressible continuum models. Finally, we briefly discuss the potential challenges with extending these models to describe nonlocal flows.

II. MODELS

In this section we will briefly review several models of compressible granular flows. These models are implemented using the mass and momentum continuity equations. The basic mass continuity equation for granular flows is

$$\frac{\partial \phi}{\partial t} + (\nabla \phi) \cdot \mathbf{u} = -\phi(\nabla \cdot \mathbf{u}), \tag{1}$$

where ϕ is the packing fraction, t the time, and $\mathbf{u}$ the velocity vector. For our systems, we consider only steady-state flows so the left term ($\partial \phi / \partial t$) equals 0. This means our results will not be applicable to systems with steady mean behavior but which display underlying transient phenomena, such as pressure waves in fluidized beds [26,27].

The momentum continuity equation is given by

$$\rho_s \phi \left(\frac{\partial \mathbf{u}}{\partial t} + \mathbf{u} \cdot \nabla \mathbf{u} \right) = -\nabla P + \nabla \cdot \boldsymbol{\sigma}' + \rho_s \phi \mathbf{g}, \tag{2}$$

where ρ_s is the particle density, **g** the gravity vector, $\boldsymbol{\sigma}'$ the deviatoric stress tensor defined as $\boldsymbol{\sigma} = \boldsymbol{\sigma}' - P\delta_{ij}$ where $\boldsymbol{\sigma}$ is the stress tensor and P the pressure, $P = -Tr(\boldsymbol{\sigma})/n$ where n is the number of dimensions (in this work $n = 3$).

Some nonlocal granular flow models introduce additional balances [4,5,28] to describe new variables, such as granular fluidity or granular temperature. However, the following models are all local, relating stress (and velocity divergence) only to local flow properties. As such, only the above equations are necessary to understand their approaches.

A. Incompressible $\mu(I)$ rheology (IMUIR)

The $\mu(I)$ model represents a significant development when modeling dense granular flows [2,29,30]. This model says that μ is described as a direct function of the inertial number I:

$$\mu(I) = \frac{|\sigma|}{P} = \mu_s + \frac{\mu_2 - \mu_s}{I_0/I + 1}, \tag{3}$$

with I_0, μ_2, and μ_s being fitted constants dependent on particle properties, with μ_s being the static yield criterion, which represents the theoretical minimum stress ratio below which flow ceases. In practice, flow is still observed frequently when $\mu < \mu_s$, but this is not captured by the $\mu(I)$ model. Some form of creep flow may be introduced to the $\mu(I)$ model when it is regularized to ensure numerical stability [13,18,20], but the physical basis for these changes is unclear.

In the above, $|\sigma|$ is the equivalent shear stress, defined as $(\sum_i \sum_j 0.5\sigma'_{ij}\sigma'_{ij})^{0.5}$, and the inertial number is defined as

$$I = |\dot{\gamma}|d\sqrt{\rho_s/P}, \tag{4}$$

where $|\dot{\gamma}|$ is the equivalent shear rate and d the local average diameter. The equivalent shear rate is defined by $|\dot{\gamma}| = (\sum_i \sum_j 2D'_{ij}D'_{ij})^{0.5}$, where $\mathbf{D}' = \mathbf{D} - \text{tr}(\mathbf{D})/n$, $D_{ij} = (\dot{\gamma}_{ij} + \dot{\gamma}_{ji})/2$ and $\dot{\gamma}_{ij}$ are the components of the shear rate tensor.

The incompressible form of the $\mu(I)$ rheology (here termed IMUIR) is obtained by combining Eq. (3) with the alignment criterion

$$\frac{\boldsymbol{\sigma}'}{|\sigma|} = \frac{2\mathbf{D}'}{|\dot{\gamma}|}, \tag{5}$$

and assuming incompressibility ($\nabla \cdot \mathbf{u} = 0$) and uniform density ($\phi = $ const).

The IMUIR model has had some success in capturing key aspects of granular flows, including channel flow [2], column collapse [13], rotating square drums [20] and even hopper discharge [14,15]. Despite its successes, IMUIR is not well posed for the full range of I values [17,18], nor does it capture compressibility or nonlocal effects. IMUIR will not be discussed in depth in this work. However, the approach forms a key basis for subsequent rheological models which are of interest to this work.

B. $\phi(I)$ relationship

The $\phi(I)$ relationship describes the packing fraction ϕ, as a function of I[1]. It provides a simple way of characterizing granular packing. While the original work suggested a linear dependence of ϕ on I, later works have proposed alternate forms [31,32]. Here we use a power law,

$$\phi = \phi_s - AI^a, \tag{6}$$

where A, a, and ϕ_s are fitted constants, with ϕ_s representing a maximum packing fraction as $I \rightarrow 0$.

The $\phi(I)$ relationship has been validated in both 2D and 3D planar shear flows [1,31,32]. In more complex geometries $\phi(I)$ is a reasonable approximation for regions where $\phi < \phi_s$, but in regions where $\mu < \mu_s$, the relationship does not apply [8,9]. It may be possible to model flow accurately while neglecting packing variations (and potentially stress variations) in regions where $\mu < \mu_s$,

but in many systems it will not be known *a priori* whether behavior in these regions is important. Therefore it is important to develop models capable of fully describing the flow throughout the domain.

$\phi(I)$, and $\mu(I)$ have been analytically solved to obtain packing and flow profiles in vertical chute and pipe flows [33], both of which are simple isochoric flows. It's unclear whether this approach can be extended to more complex isochoric flows, and for unsteady or nonisochoric flows $\nabla \cdot \mathbf{u}$ must also be modeled. Various compressible granular flow models have been developed that incorporate $\phi(I)$ in such a way as to ensure that as $\nabla \cdot \mathbf{u} \to 0$, $\phi \to \phi(I)$. Below we outline some of the developed approaches.

C. Dilatancy law (DL)

When we refer to dilatancy law (DL) we refer to a specific approach used to model transient shifts in ϕ developed out of soil mechanics [23,34]. This approach introduces the dilatancy angle (ψ) to relate deformation to changes in volume. For planar shear starting from rest, ψ is the angle of motion relative to the horizontal arising from displacement, with $d\Delta Y = \tan(\psi)d\Delta X$ where $d\Delta Y$ and $d\Delta X$ are the vertical and horizontal displacement. This relationship is used to link ψ to the normal shear rate and, in conjunction with the mass continuity, the transient change in ϕ. Thus, ψ characterizes the motion arising due to the material dilating to allow flow. This definition of ψ is specific to planar shear. A generalized 3D form of the dilatancy angle is given by [23]

$$\sin \psi = \frac{2}{3} \frac{\nabla \cdot \mathbf{u}}{|\dot{\gamma}|}. \tag{7}$$

The DL model describes stress with the expression

$$|\sigma| = P \sin(\delta + \psi), \tag{8}$$

with δ being the internal angle of friction. Provided ψ is small, it is typical to take $\sin(\delta + \psi) = \sin \delta + \sin \psi$ where $\sin \delta = \mu_s$ and $\sin \psi \approx \psi$. In some cases, μ_s is replaced with $\mu(I)$ [24,34].

This leaves ψ as an unknown. Roux and Radjai [35] suggested the now common closure

$$\sin \psi = \psi = K(\phi - \phi_s), \tag{9}$$

wherein ψ is linearized about the critical packing fraction ϕ_s, which is the packing obtained for steady isochoric flow. As with μ_s, shear rate dependence is incorporated by replacing ϕ_s with $\phi(I)$. This gives the following two expressions:

$$\mu = \mu(I) + K(\phi - \phi(I)), \tag{10a}$$

$$K[\phi - \phi(I)] = \frac{2}{3} \frac{\nabla \cdot \mathbf{u}}{|\dot{\gamma}|}, \tag{10b}$$

which are combined with the alignment criterion [Eq. (5)] to close the equations. The above set of equations provides a simple modification to $\mu(I)$ that may describe transient and compressibility effects, but collapses to the result for $\phi(I)$ and $\mu(I)$ for steady, isochoric flows.

DL has been used to model dry avalanche flows [24]. However, it has been more widely used for modeling thin, transient avalanche flow of granules immersed in fluids [34,36–39], with the equations slightly modified to account for fluid-solid interactions.

D. Compressible $\mu(I)$ rheology (CMUIR)

The compressible $\mu(I)$ rheology, here termed CMUIR, is an approach that deliberately preserves much of the form of the $\mu(I)$ model [22,40]. For CMUIR, I is modified by replacing P with P_{eqb}, the

"equilibrium" pressure. It is then possible to rearrange $\mu(I)$ and $\phi(I)$ to obtain $\mu(\phi)$ and $P_{\text{eqb}}(\phi, |\dot{\gamma}|)$. The following expressions are then defined:

$$\mu(\phi) = \frac{|\sigma|}{P_{\text{eqb}}}, \tag{11a}$$

$$P = P_{\text{eqb}}\left(1 - \mu_b(\phi)\frac{2\boldsymbol{\nabla} \cdot \mathbf{u}}{|\dot{\gamma}|}\right). \tag{11b}$$

$\mu_b(\phi)$ represents an additional factor that, while expected to be dependent on ϕ, has been previously treated as a constant.

Equations (11a) and (11b), when combined with the alignment criterion, provide descriptions of the current pressure and stress. These are substituted into Eq. (2), which along with Eq. (1), provides a complete system of equations to solve. For flows which at steady state are isochoric, the $\phi(I)$ and $\mu(I)$ relationships are recovered.

CMUIR has been shown to be well posed for the full range of I values, provided $\mu_b > 1 - 7\mu/6$ [22]. In gravityless planar shear, CMUIR has been shown to capture transient wave features that were observed to propagate during steady flow [40]. CMUIR has not yet been applied to model more complex flows.

E. Compressible I-dependent rheology (CIDR)

The compressible I-dependent rheology, CIDR [21,41], is an approach to develop a well-posed dilatant continuum model. There are two fundamental equations underlining the model. First, a yield function is used to govern the stress response in yielding granular material:

$$|\sigma| = Y(P, \phi, I). \tag{12}$$

Here $Y(P, \phi, I)$ is a function which defines $|\sigma|$ as a function of pressure, packing fraction, and inertial number. Second, a flow rule is used to close the continuity equation:

$$\boldsymbol{\nabla} \cdot \mathbf{u} = f(P, \phi, I)|\dot{\gamma}|. \tag{13}$$

Here $f(P, \phi, I)$, the flow rule function, provides dependence on P, ϕ, and I. While not explicitly written as such, it should be apparent that IMUIR and CMUIR could be written to follow a similar form, though the specific flow rule and yield functions would incorporate dependence on different parameters.

To relate $Y(P, \phi, I)$ to $f(P, \phi, I)$ and ensure the resulting model is well posed, CIDR uses the following criteria [21]:

$$\frac{\partial Y}{\partial P} - \frac{I}{2P}\frac{\partial Y}{\partial I} = f + I\frac{\partial f}{\partial I}, \tag{14a}$$

$$\frac{\partial Y}{\partial I} > 0, \tag{14b}$$

$$\frac{\partial f}{\partial P} - \frac{I}{2P}\frac{\partial f}{\partial I} > 0. \tag{14c}$$

The resulting model is then applied in much the same way as CMUIR, with the alignment condition and yield function being used to describe the stress response in Eq. (2) and the flow rule being used to define pressure. Using these equations, Eqs. (1) and (2) can be solved transiently to reach the steady response in any system.

The original CIDR description (hereafter referred to as oCIDR) [21], suggested the following form for the yield and flow rule functions:

$$Y(P, \phi, I) = \alpha(I)P - \frac{P^2}{C(\phi)}, \tag{15a}$$

$$f(P, \phi, I) = \beta(I) - \frac{2P}{C(\phi)}. \tag{15b}$$

The forms of the functions $\alpha(I)$ and $\beta(I)$ are chosen such that, in the incompressible case, the yield function collapses to Eq. (3). $C(\phi)$ is taken as a function that bounds ϕ by an arbitrarily chosen $\phi_{\min}$ and $\phi_{\max}$ with $C(\phi_{\min}) = 0$ and $C(\phi_{\max}) = \infty$ (when considering a chute flow they used $\phi_{\min} = 0.5$ and $\phi_{\max} = 0.6$).

Unlike the other compressible flow models considered, this formulation does not attempt to directly incorporate $\phi(I)$. The yield function is based on a critical state soil mechanics yield function, which is used to derive the flow rule. In the isochoric case $C(\phi) = 2P/\beta(I)$ which can be rearranged to give $\phi(P, I)$ and hence is similar to the $\phi(I)$ model. However, for flows where P is not uniform it seems unlikely the $\phi(I)$ response would be recovered.

As noted, CIDR represents an approach to defining well-posed continuum equations. Unsurprisingly oCIDR is not the only formulation. Another version, the inertial-CIDR (iCIDR) model has also been proposed [25]. This model aims to explicitly recreate the $\phi(I)$ and $\mu(I)$ relationships while utilizing the well-posed framework of the CIDR approach. Specifically, they suggest the yield and flow rule functions:

$$Y(P, \phi, I) = \mu(\Psi(\phi))\frac{I}{\Psi(\phi)}P, \tag{16a}$$

$$f(\phi, I) = \frac{1}{4}\mu(\Psi(\phi))\left[\frac{I}{\Psi(\phi)} - \frac{\Psi(\phi)}{I}\right], \tag{16b}$$

where $\Psi(\phi)$ is the inverted $\phi(I)$ relationship, so I as a function of ϕ. It should be apparent that, in the incompressible case $I = \Psi(\phi)$, hence $f(\phi, I) = 0$ and the $\mu(I)$ and $\phi(I)$ relations are recovered.

The two forms of CIDR have seen limited application. The oCIDR model has been applied to inclined plane flows [21] and to planar shear flows [41], where it was able to capture the same transient wave behavior as the CMUIR model. The iCIDR model has been applied to planar shear where it accurately described the collapse of a perturbed flow field towards its steady flow profile [25].

III. METHODS

DEM simulations were used to test the above models in complex, nonisochoric flows. Simulations were run using the open source software LIGGGHTS [42] using a 3D soft sphere approach and a Hookean contact model. Particles properties were set to ensure rigid particles (using the criterion $K_n/Pd > 10^4$ where K_n is the normal spring constant [43]). A size distribution $d_m \pm 20\%$, where d_m is the overall numerical mean diameter, was implemented to prevent crystallization. Specifics on the DEM approach, including the chosen particle properties, are listed in the Supplemental Material [44].

While the focus of this work is on examining nonisochoric flows, we also ran simulations in a complex isochoric flow geometry. This geometry, shown in Fig. 1, is a constant volume, split bottom shear cell. The geometry was used to help examine the alignment criterion (as outlined in Sec. IV B). The geometry was filled with 29 600 particles and run with gravitational acceleration (G) applied along the z axis set to $G = 2.07 \times 10^{-7} K_n d_m/m$ (K_n is the spring constant and m the particle mass) for all simulations. The top wall is stationary, and the bottom wall is split in two with each half moving at different velocities ($V_{y,1}$ and $V_{y,2}$). Four simulations were run using different values for $V_{y,1}$ and $V_{y,2}$ (the exact values used are given in the Supplemental Material [44]).
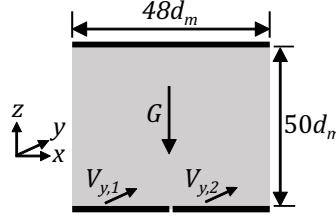
FIG. 1. 2D Diagram of a 3D split bottom shear cell. The geometry is periodic along the x and y axis and is $12d_m$ wide along the y axis.

Aside from the split bottom shear cell our analysis is primarily restricted to complex geometries in which, at steady state, flow is nonisochoric and transient in a Lagrangian sense. The geometries considered are shown in Fig. 2. These are the pseudo-2D hopper [Fig. 2(a)], the vertical chute with hemicylindrical inserts [Fig. 2(b)] and the vertical chute with wedge inserts [Fig. 2(c)]. For the pseudo-2D hopper (the simulations for which were taken directly from [8]), we considered hoppers of two different widths W and two different outlet widths OW. The hoppers were filled with a number of particles (N_o) proportional to their width, with $N_o = 2660W/d_m$, to ensure a consistent height of roughly $200d_m$. The system was periodic along the y axis and along the z axis, with particles $62.5d_m$ below the outlet being recycled to well above the top of the bed. The gravitational acceleration was applied along the z axis, with $G = 4.05 \times 10^{-7} K_n d_m/m$. The walls were smooth but frictional with properties identical to the particles. For the two chute geometries, three different lengths L were considered. The geometry was periodic along the z and y axis. N_o was almost proportional to L, with an adjustment made to account for the volume occupied by the insert, $N_o = 12.3(50L - A_{\text{insert}}/d_m^2)$ (rounded to the nearest particle). A_{insert} is the cross-sectional area of the inserts on the xz plane. G was defined as $G = 2.07 \times 10^{-7} K_n d_m/m$ and applied along the z axis. The walls were rough, being composed of fixed, densely packed particles with a diameter d_m and properties identical to the flowing particles. Dimensions are defined based on the center of mass of the wall particles, though some parts of these particles will protrude further into the flow.

Properties such as particle position, velocity and contact force, were extracted from the DEM simulations using coarse graining [45–47]. We use our approach as in [8,48], with a Lucy function as the weighting function using a width of $1.5d_m$ and a cutoff of $3d_m$. This cutoff was kept $1.5d_{\text{max}}/2$ from the walls for all analysis. In all cases we incorporate both spatial and temporal averaging. We average five values along the y axis and average over 400 discrete time steps (each 100 000 DEM time steps apart). When coarse graining in the split bottom shear cell and the vertical chute with hemicylindrical or wedge inserts geometries, we consider 29 positions along the z axis. In the split bottom shear cell geometry we consider 16 positions along the x axis, while in the chute with inserts geometries we analyze $L/3d_m$ positions along the x axis. For the hoppers, we analyze 30 positions along the centerline of the system ($x = 0$) starting at the outlet ($z = 0$) and running up to $z = 37.5d_m$.
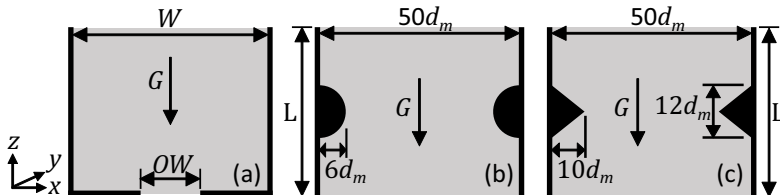

FIG. 2. 2D diagrams of the 3D geometries simulated, showing the x and z axes. Panel (a) is a pseudo-2D hopper, (b) is a vertical chute with hemicylindrical inserts, and (c) is a vertical chute with wedge inserts. The width of the chute geometries along the y axis was $12d_m$, and the hopper was $10d_m$.
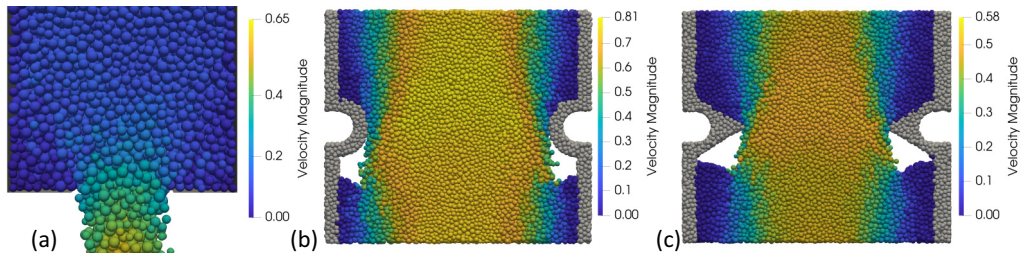
FIG. 3. Typical flow profiles obtained in the pseudo-2D hopper (a), vertical chute with hemicylindrical inserts (b), and vertical chute with wedge inserts (c) geometries. Particles are shown with their color scaled based on their velocity magnitude (in m s^{-1}). In (a) the smooth walls are shown in gray. The insert geometries shown in (b) and (c) have walls composed of fixed particles, which are shown in gray. The hopper data are cropped, showing only the domain near the outlet.

Figure 3 shows a snapshot of the flow in each nonisochoric flow geometry (shown for $L = 48d_m$). It can be seen that immediately after the inserts the flow becomes detached from the wall-forming large void regions (the size of which grew as L was increased). This is different from what would be observed for a fluid, where density remains uniform and recirculation zones form. This behavior has also been noted for hoppers with internal inserts [49]. The behavior is interesting as it is unclear if any current continuum model for dense granular flow can capture these voids, certainly none of the models considered here make an allowance for their presence. However, while interesting, these detached regions are not the focus of our analysis and we restrict our analysis to regions fully occupied by flow. The criterion used to restrict our analysis was $\phi > 0.51$; any regions where this criterion was not met were not considered.

IV. RESULTS

In this section, we first examine some of the flow properties coarse grained from our DEM simulations. We then look at whether previously observed relationships, namely, $\phi(I)$, $\mu(I)$, $\phi(\mu)$, and the alignment criterion, are recovered in these systems.

A. $\phi(I)$, $\mu(I)$, and $\phi(\mu)$ relations

Figure 4 shows the $\phi(I)$, $\mu(I)$, and $\phi(\mu)$ relationships in the split bottom shear cell geometry, along with the results of previous simulations of shear cells, shear cells with gravity, and vertical chutes (these are taken from [8]). All four geometries exhibit the typical $\mu(I)$, $\phi(I)$, and $\phi(\mu)$ responses previously seen in isochoric systems. The $\phi(I)$, $\mu(I)$, and $\phi(\mu)$ relationships were fitted to the shear cell data, and are shown as black lines. To fit the $\phi(\mu)$ data, we use the function

$$\phi(\mu) = \mu B \left(\frac{\mu}{C - \mu} \right)^D + \phi_{\max}. \tag{17}$$

This empirical equation provided a good fit over the range of I values considered. The fitted coefficients for the $\mu(I)$ response were $\mu_s = 0.3722$, $\mu_2 = 1.079$ and $I_0 = 0.7630$, for the $\phi(I)$ response $\phi_s = 0.5985$, $A = 0.1305$, and $a = 0.8156$, and for the $\phi(\mu)$ response $B = -0.1767$, $C = 0.8916$, $D = 0.1741$, and $\phi_{\max} = 0.6593$.

Next, for each nonisochoric flow simulated the $\mu(I)$, $\phi(I)$, and $\mu(\phi)$ relations are examined, as shown in Fig. 5. The results for the pseudo-2D hopper [Figs. 5(a)–5(c)] have been shown in our prior work [8]. When I is high, the $\phi(I)$ and $\mu(I)$ responses are recovered; at low I, a different response was observed. However, unlike the results in Fig. 4(c), we do not see a collapse onto the $\phi(\mu)$ relationship, and instead observe a range of responses when $\phi > \phi_s$. Previously, we theorized
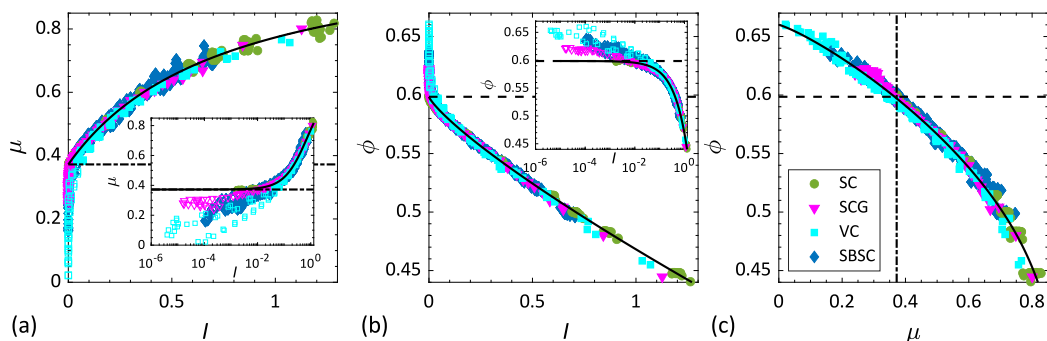
FIG. 4. Results of the DEM simulations for (a) μ vs I, (b) ϕ vs I, and (c) ϕ vs μ for the shear cell, shear cell with gravity, vertical chute, and split bottom shear cell simulations (multiple simulations were run in each geometry but are shown as the same color for simplicity). The solid black lines show the fitted $\mu(I)$ [Eq. (3)], $\phi(I)$ [Eq. (6)], and $\phi(\mu)$ [Eq. (17)] relationships, while the dashed lines mark the position of μ_s and ϕ_s. The $\mu(I)$ and $\phi(I)$ equations are fitted to the shear cell data while $\phi(\mu)$ is fitted to the full dataset. The insets show $\mu(I)$ and $\phi(I)$ with the x axis on a log scale. Points where $\mu < \mu_s$ (a) or $\phi > \phi_s$ (b) are hollow.

the breakdown in the $\phi(\mu)$ relation arose due to the hopper being a geometry which, even at steady state is transient in a Lagrangian sense, displaying nonisochoric flow.

If we now look at the vertical chute with hemicylindrical inserts simulations [Figs. 5(d)–5(f)], we can see very similar behavior occurring. The chutes with inserts geometries were simulated for three different lengths L. As the geometries are periodic along the z axis, they can be considered as infinite chutes with a series of repeating inserts protruding regularly from the walls. As we reduce L the spacing between each insert decreases. We plot only the results for the hemicylindrical inserts geometry as the wedge inserts geometry produced very similar behavior (this is shown in the Supplemental Material [44]). In the shortest case ($L = 12d_m$) there is no space between each insert. Particles close to the wall are effectively static, resulting in a narrow chute forming through the center, and the inserts behaving akin to a flat wall. Thus, for this case we recover an identical response to a chute. We obtain the $\phi(I)$ and $\mu(I)$ responses in regions where $\phi < \phi_s$ and $\mu > \mu_s$ and the $\phi(\mu)$ response is observed throughout the region analyzed.

However, as we increase L, and so the spacing between inserts, the flow is able to deform around the inserts. The flow becomes "less isochoric." For $L = 24d_m$ we still recover $\phi(I)$ and $\mu(I)$ for high I. However, we begin to see deviation from $\phi(\mu)$ at low μ values. In Fig. 5(f) we see clusters of points at nearly constant ϕ (with each cluster corresponding to different x positions). These points spread over a range of μ values, as μ begins to vary significantly along the z axis (i.e., in the direction of flow).

Finally, for the longest case $L = 48d_m$ we observe that μ and ϕ follow the $\mu(I)$ and $\phi(I)$ relationships in high I regions of flow. In the region $0.05 < I < 0.2$, μ increases slightly above the the $\mu(I)$ relationship, but the difference is small. However, in dense regions, the deviation from the $\phi(\mu)$ response is significant, with large variations in μ along the z axis, and smaller but still noticeable variation in ϕ. Large variations in the flow profile occur as flow deforms around the inserts.

Our results show that in these nonisochoric flows, in regions where I is high, the $\mu(I)$ and $\phi(I)$ relations will still be recovered. However, unlike in isochoric flows, the system does not behave consistently with the $\phi(\mu)$ model in dense regions. This is consistent with our prior observations that in nonisochoric flows ϕ and μ evolve at different rates [8]. Deformations in the flow around the insert cause variations in μ. As ϕ evolves more slowly than μ, it lags μ and $\phi(\mu)$ is not properly recovered. For our subsequent analysis we restrict the chute with inserts geometries considered

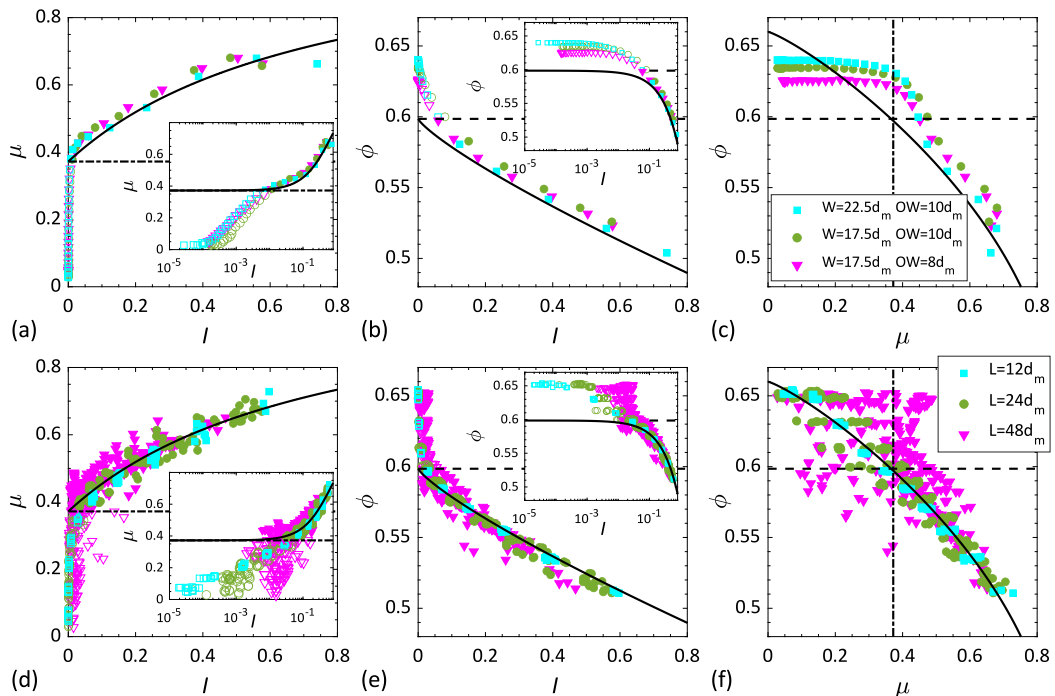FIG. 5. μ vs I, ϕ vs I, and ϕ vs μ, shown for simulations of pseudo-2D hoppers (a–c) and vertical chute with hemicylindrical inserts (d–f) geometries. Solid black line(s) show the $\mu(I)$, $\phi(I)$, and $\phi(\mu)$ relations, while dashed lines mark the position of μ_s and ϕ_s. Inserts show μ vs I and ϕ vs I with the x axis plotted on a log scale. Points where $\mu < \mu_s$ (a, d) or $\phi > \phi_s$ (b, e) are hollow.

to the longest geometry ($L = 48d_m$) as this displayed the greatest deviation from isochoric flow behavior. We still consider all three hoppers simulated.

B. Alignment criterion

The alignment criterion [Eq. (5)] is used in most local granular flow models, including those detailed in the Sec. II, to relate the deviatoric stress tensor components to the deviatoric strain rate tensor components, along with $|\sigma|$ and $|\dot{\gamma}|$. $|\sigma|$ is then defined as function of $|\dot{\gamma}|$ (and other variables), thus allowing the stress to be resolved. This approach has also been used for at least one nonlocal flow model [11]. Here we first examine the alignment criterion in isochoric systems. For this analysis we want an isochoric flow geometry which exhibits local and nonlocal regions, with multiple nonnegligible components of the $\boldsymbol{\sigma}'$ and $\mathbf{D}'$ tensors, and where $|\dot{\gamma}|$ is always nonnegligible.

For the three isochoric flow geometries taken from [8] (the shear cell, shear cell with gravity and vertical chute), the $\boldsymbol{\sigma}'$ and $\mathbf{D}'$ tensors are dominated by a single component. When plotting this component the alignment criterion will collapse onto 1 or -1. As such, none of these geometries is suitable for this analysis.

To examine a complex isochoric flow, we instead simulated the split bottom shear cell geometry (Fig. 1). This system gives us two relevant tensor components (yx and yz). We do also observe that $\sigma_{xx} \neq \sigma_{yy} \neq \sigma_{zz} \neq P$ even when $\dot{\gamma}_{xx} \approx \dot{\gamma}_{yy} \approx \dot{\gamma}_{zz} \approx 0$. Hence, there is a minor contribution to $|\sigma|$ from the normal stresses, which is also seen in the other isochoric systems, but this contribution is not significant. These are plotted in Fig. 6, along with a black line showing the expected result of the alignment criterion. The symbols are colored such that where $I > 0.1$, the symbols are red and where $I < 0.1$ the symbols are blue. The criterion $I > 0.1$ is used to approximately separate regions that
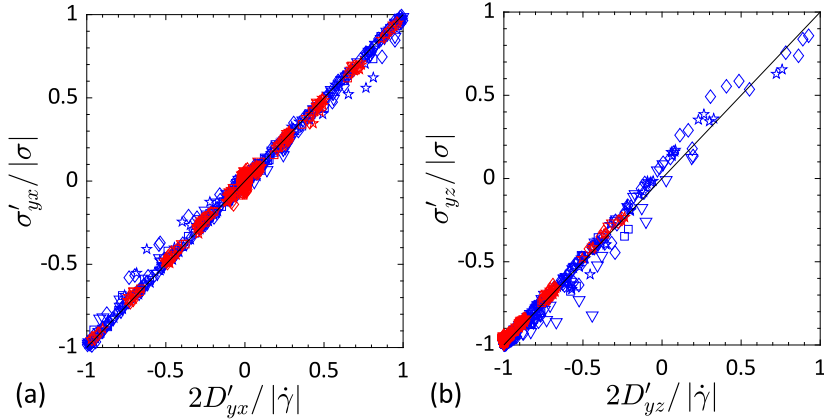
FIG. 6. Alignment criterion for isochoric, split bottom shear cell flow. Panel (a) shows *yx* and (b) *yz*. Different symbols denote simulations with different wall velocities.

are likely "local" from those that are "nonlocal." Figure 6 shows that in both high and low I regions, the components of the deviatoric stress tensor fall on the black line, indicating that they are directly proportional to the components of the deviatoric stain rate tensor. Thus, despite different tensor components contributing to varying extents in local and nonlocal regions, the alignment criterion holds throughout the system in this complex, isochoric flow.

In Fig. 7 we plot the alignment criterion for the primary stress components (*zx*, *xx* and *zz*) in our nonisochoric systems. As before, we color the symbols such that where $I > 0.1$ the symbols are red and where $I < 0.1$ the symbols are blue. In a nonisochoric flow it is not clear whether this simple criterion accurately demarcates the local and nonlocal regions of the flow. However, Fig. 5 indicates that deviations from $\phi(I)$ and $\mu(I)$ generally occur where $I < 0.1$, and hence the color coding is likely still relevant. Figure 7 shows that in nonisochoric flows where $I > 0.1$, the alignment criterion holds quite well. However, where $I < 0.1$, there is no apparent correlation observed between the deviatoric stress and strain rate tensor components. This observation suggests that the alignment criterion does not apply to dense, nonisochoric flows. Since the breakdown of the alignment criterion is only observed in dense, low I, regions, it may be associated with nonlocality. However, for isochoric flows, as Fig. 6 shows, the alignment criterion holds well in nonlocal regions. Therefore, the deviation seen in Fig. 7 is likely a nonisochoric flow phenomena.
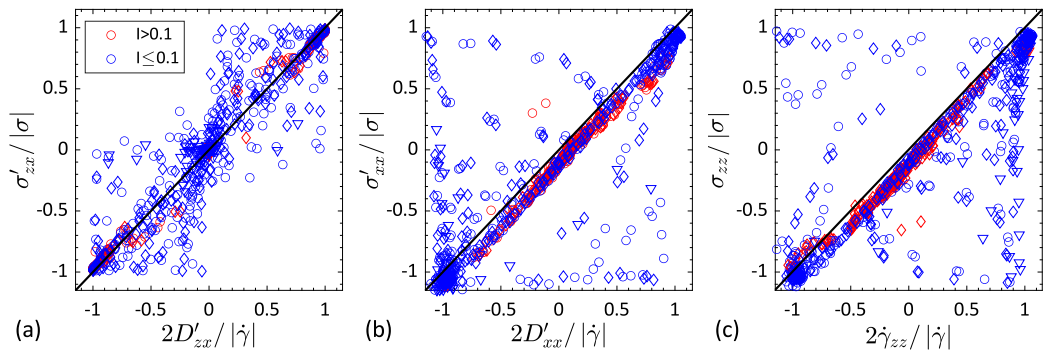

FIG. 7. Alignment criterion for different tensor components in hopper ($\triangledown$), chute with hemicylindrical inserts ($\diamondsuit$) and chute with wedge inserts ($\diamondsuit$) geometries. Panel (a) shows *zx*, (b) *xx*, and (c) *zz*.
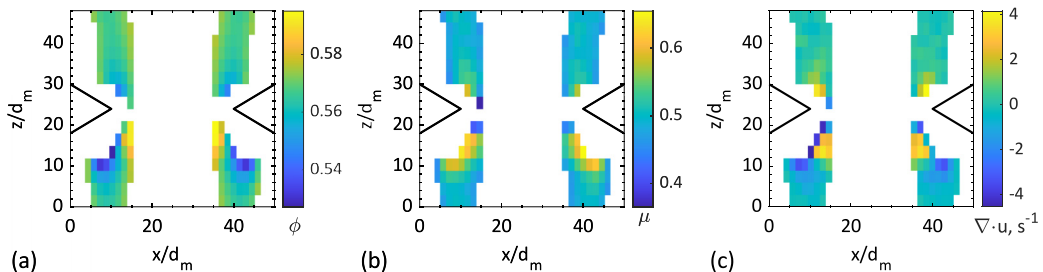
FIG. 8. (a) ϕ, (b) μ, and (c) $\nabla \cdot \mathbf{u}$ in the vertical chute with wedge inserts geometry for regions where $I > 0.1$. Regions in white are those not considered or analyzed due to not meeting this cutoff, being too close to the walls, or having $\phi < 0.5$. The black lines show the positions of the inserts.

There are an infinite number of isochoric and nonisochoric flows and examining the alignment criterion in all of them is obviously unfeasible. However, the results obtained suggest that, while the alignment criterion holds across a range of isochoric flows, it does not hold in nonisochoric systems where I is low and flow is likely nonlocal.

V. DISCUSSION

In Sec. V A we seek to evaluate the performance of the different compressible flow models considered. We do this by direct comparison between the local values of stress and velocity divergence coarse grained from our DEM simulations, and with the values predicted by our different models, using DEM inputs to solve for stress and velocity divergence. If the models capture the rheology of the flow, the model values and the DEM values will match. Alongside this analysis, we consider an alternate approach based around integration of the mass continuity equation. This is done to allow us to evaluate the ability of the models to recover the observed trends in packing, even if they cannot perfectly match the DEM results. Finally, we consider potential ways of improving upon the existing compressible flow models.

In Sec. V B we comment on some of the potential issues with extending the compressible flow models into nonlocal flow regions.

A. Local model analysis

Now that we have established the behavior of our different geometries, we next examine the different dilatant models. The different models examined are all local. Additionally, some of the models are not valid if $\phi > \phi_s$. As such we restrict our analysis to regions where $I > 0.1$ (or close to 0.1, as is discussed later) and $\phi < \phi_s$. This high I cutoff should ensure flow remains within the intermediate regime [50]. The region of flow considered for the vertical chute with wedge inserts geometry is shown in Fig. 8, plotted as color maps of ϕ, μ, and $\nabla \cdot \mathbf{u}$. The region considered for the hemicylindrical inserts geometry was similar. The criterion $\mu = \mu_s$ has been used to previously separate out nonlocal and local regions of flow in isochoric systems [4,11]. For nonisochoric flows, it is unclear how well this transition is defined (see Fig. 5). Hence the use of an I-based cutoff to ensure flow is local. This is an inherent limitation of local models, since it restricts the regions of flow we can analyze and indeed restricts their general application to only a limited range of flow types.

1. Prediction for $\nabla \cdot \mathbf{u}$ velocity divergence

Initially, we consider the different models from the perspective of their predicted velocity divergence. For this we will focus on CMUIR, iCIDR, and DL. oCIDR is difficult to examine with the same methodology, largely because the $C(\phi)$ function contains multiple fitting parameters,
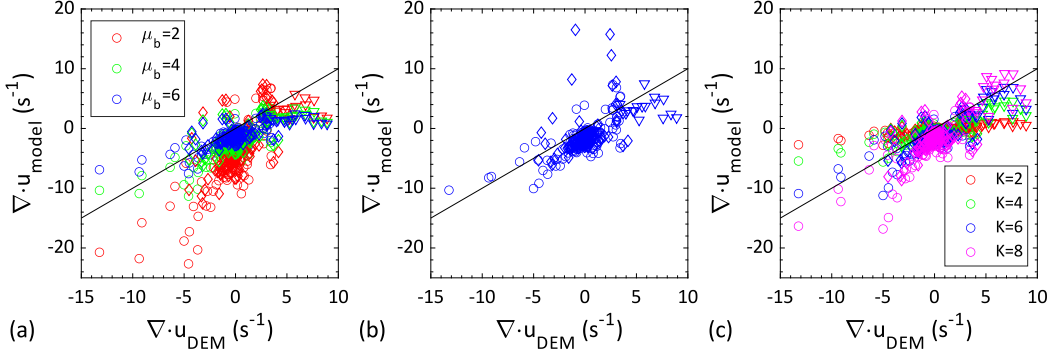
FIG. 9. DEM $\nabla \cdot \mathbf{u}$ vs $\nabla \cdot \mathbf{u}$ predicted by (a) CMUIR, (b) iCIDR, and (c) DL in the pseudo-2D hopper ($\triangledown$), chute with hemicylindrical inserts ($\circ$) and chute with wedge inserts ($\lozenge$) geometries. Data are shown for regions where ($I > 0.1$). The black line shows the ideal result ($\nabla \cdot \mathbf{u}_{\text{model}} = \nabla \cdot \mathbf{u}_{\text{DEM}}$).

compared with the single fitting parameter of CMUIR or DL. We will discuss this model in the subsequent section on the prediction for $|\sigma|$. For each model considered, we take properties obtained from the DEM simulations and use them to calculate $\nabla \cdot \mathbf{u}$ [by rearranging Eq. (11b) and Eq. (10) for $\nabla \cdot \mathbf{u}$], using multiple values of the unknown parameters μ_b (for CMUIR) and K (for DL). The predicted $\nabla \cdot \mathbf{u}$ ($\nabla \cdot \mathbf{u}_{\text{model}}$) is then compared with the coarse grained $\nabla \cdot \mathbf{u}$ ($\nabla \cdot \mathbf{u}_{\text{DEM}}$) as shown in Fig. 9. For CMUIR we inverted Eq. (17) for $\mu(\phi)$ rather than combining $\mu(I)$ and $\phi(I)$ as it provides identical results when $\phi < \phi_s$.

Figure 9 shows that there is a large amount of scatter for all of the models, with no model having $\nabla \cdot \mathbf{u}_{\text{model}}$ collapse smoothly onto $\nabla \cdot \mathbf{u}_{\text{DEM}}$. For CMUIR and DL, the predicted $\nabla \cdot \mathbf{u}_{\text{model}}$ best matches $\nabla \cdot \mathbf{u}_{\text{DEM}}$ when $\mu_b \approx 4$ and $K \approx 6$. This is somewhat subjective, and even for these values the agreement is poor. iCIDR lacks a fitting parameter to vary and performs similarly to the other two models. For iCIDR there are a few points from the wedge inserts geometry ($\lozenge$) where $\nabla \cdot \mathbf{u}_{\text{model}}$ is around 10–20 while $\nabla \cdot \mathbf{u}_{\text{DEM}} \approx 0$. These are points close to the centerline where ϕ is large. For all three models we can see that when $\nabla \cdot \mathbf{u}_{\text{DEM}} \approx 0$ the values of $\nabla \cdot \mathbf{u}_{\text{model}}$ are typically under predicted, with points being clustered below the black line. Based purely on Fig. 9 the different compressible models perform poorly, being unable to properly recover the velocity divergence in the simulated geometries.

To examine these models further, we use them to integrate the mass continuity equation at a constant x position along the z axis and so recover ϕ. We consider the chute with inserts geometries. In these geometries stress, velocity, and packing were evaluated at different x and z positions. We take data at two specific x positions ($x = 11.76 d_m$ and $x = 38.24 d_m$ for the hemicylindrical inserts chute and $x = 14.7 d_m$ and $x = 35.3 d_m$ for the wedge inserts chute, where $x = 0$ is the left wall) and using the mass continuity equation [Eq. (1)], evaluate ϕ along the z axis. To do so, we rearrange Eq. (1) considering that the systems are steady ($\partial/\partial t = 0$) and uniform along y ($\partial/\partial y = 0$):

$$u_z \frac{\partial \phi}{\partial z} = -u_x \frac{\partial \phi}{\partial x} - \phi \nabla \cdot \mathbf{u}. \tag{18}$$

Equation (18) is integrated numerically (we used Euler's method), taking the highest point analyzed on the z axis as an initial value and solving in the direction of flow. We take $\partial \phi / \partial x$ from our DEM simulations and calculate $\nabla \cdot \mathbf{u}$ using the different models. All necessary inputs to the models are taken from the DEM simulation data, excluding ϕ. For this analysis, 32 z positions were coarse grained at the specific x position considered, ensuring high spatial resolution on the necessary inputs (which were interpolated along z to allow a small step size to be used for the integration). In both chute with inserts geometries across the full z range I briefly drops down to $I = 0.06$ (for hemicylindrical inserts) or $I = 0.03$ (for wedge inserts), and hence slightly below the specified
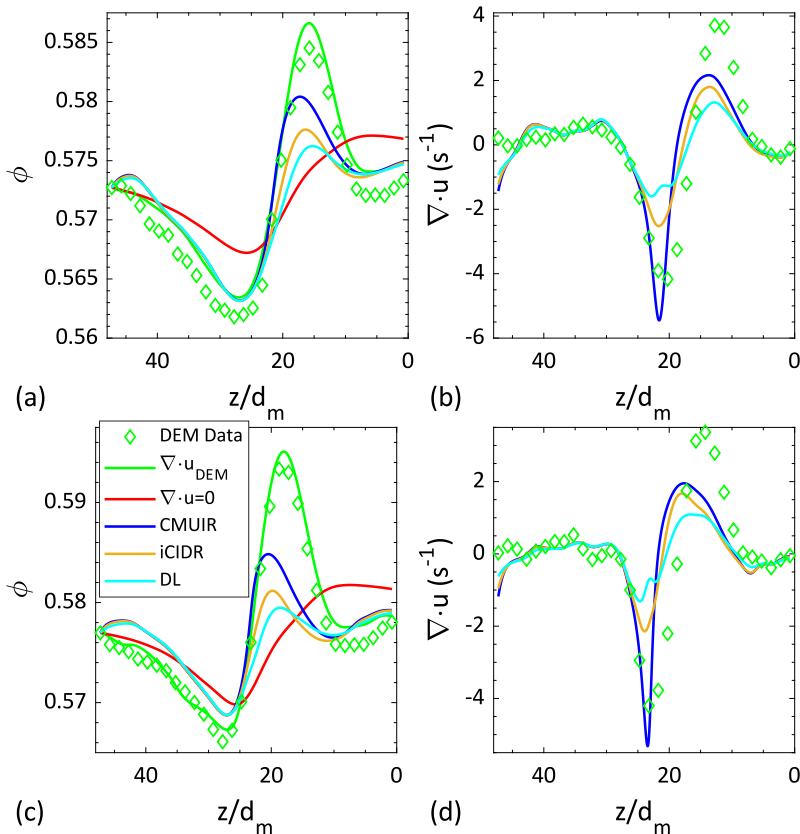
FIG. 10. Integration of mass continuity to obtain ϕ in the vertical chute with hemicylindrical (a) and wedge (c) inserts, using different models. Panels (b) and (d) show the corresponding $\nabla \cdot \mathbf{u}$. For CMUIR $\mu_b = 4$ was used and for DL $K = 6$.

threshold $I > 0.1$. However, for the majority of the z range I is close to or greater than 0.1. The minimum I values reached are not very low, and so nonlocal behavior in these regions is likely to be minimal. Furthermore, $\phi < \phi_s$ throughout the selected region, which is necessary for CMUIR and iCIDR.

The results of this analysis are shown in Fig. 10, plotted for the x position closest to the insert (the result nearer the center is similar and given in the Supplemental Material [44]). For comparison we show the results found when integrating the data using $\nabla \cdot \mathbf{u}$ taken from the simulations ($\nabla \cdot \mathbf{u}_{\text{DEM}}$) and using $\nabla \cdot \mathbf{u} = 0$. Using $\nabla \cdot \mathbf{u}_{\text{DEM}}$ to solve for ϕ results in a curve that closely matches this observed data. This provides confirmation that our coarse-grained values are accurate and conservation of mass is recovered. If we assume incompressibility and $\nabla \cdot \mathbf{u} = 0$, we get the red line, which shows a poor fit to the data. Figure 10 shows that, in both systems, ϕ decreases as we approach the insert and then increases again after the flow passes the insert. This peak is more prominent in the chute with wedge inserts compared to the chute with hemicylindrical inserts, though the difference between the maximum and minimum ϕ is similar. The peaks are clearly correlated with shifts in $\nabla \cdot \mathbf{u}$ about the inserts [Fig. 10(b)].

Looking at the predictions of the models they all capture key features of the DEM simulations, and improve on the result obtained when $\nabla \cdot \mathbf{u} = 0$. The models all capture the initial drop in ϕ, and the position of the minimum ϕ (even if they don't reach the correct minimum). In the case of the vertical chute with hemicylindrical inserts, the models align particularly well with the results
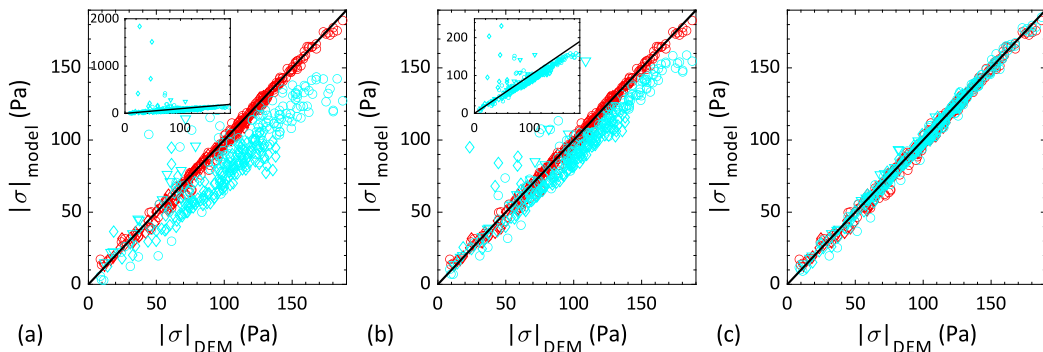
FIG. 11. DEM $|\sigma|$ vs predicted $|\sigma|$ for CMUIR (a), iCIDR (b) and DL (c). These are plotted in cyan. $|\sigma|$ predicted by IMUIR is plotted in red. Symbols are as in Fig. 7. The black line shows the ideal result ($|\sigma|_{\text{model}} = |\sigma|_{\text{DEM}}$). For (a) and (b), the data have been truncated to keep axes consistent. The inserts show the full results.

using $\nabla \cdot \mathbf{u}_{\text{DEM}}$. Similarly, all three models partially capture the subsequent rise in ϕ, though none correctly recovers the value and position of the maximum ϕ. Figures 10(b) and 10(d) show that the models correctly describe the regions where $\nabla \cdot \mathbf{u}$ is close to 0 and capture the drop in divergence about the insert. Thus, they capture some of the true behavior quite well. They don't fully capture the subsequent rise in $\nabla \cdot \mathbf{u}$, which is likely why they can't replicate the spike in ϕ. This is most notable in the chute with wedge inserts geometry with the large ϕ increase being poorly captured.

Of all the models, it is CMUIR which seems to give the best results. All the models show improvement over $\nabla \cdot \mathbf{u} = 0$, which indicates that there is potential for these models to be applied to accurately model dilatancy and packing for compressible, nonisochoric flows.

2. Prediction for |σ| equivalent shear rate

How well these different models handle dilatancy is key to determining their applicability to complex systems. However, equally important is their prediction for $|\sigma|$. All the models considered in some way modify the prediction of IMUIR, $|\sigma| = \mu(I)P$, to account for the impact of dilatancy on stress. In Fig. 11 we examine how these modifications affect the predicted $|\sigma|$ compared to the coarse grained $|\sigma|$ recovered from the simulations. Alongside the model predictions, we also include the prediction of IMUIR (red symbols). To calculate the stress using these models and minimize the impact of fitting parameters we do as follows. For DL, rather than use Eq. (10a), we instead modify the equation by substituting in Eq. (7) so $|\sigma| = P(\mu(I) + 2\nabla \cdot \mathbf{u}/3|\dot{\gamma}|)$. This allows us to examine the model's underlying assumptions regarding how dilatancy impacts stress independent of the validity of Eq. (9). For oCIDR, the multiple constants in the $C(\phi)$ expression make Eq. (15a) difficult to implement. However, given the definitions for $\alpha(I)$ and $\beta(I)$ it is possible to rearrange Eqs. (15a) and (15b) to obtain $|\sigma| = P(\mu(I) + \nabla \cdot \mathbf{u}/2|\dot{\gamma}|)$, which is effectively the value of $|\sigma|$ if Eq. (15b) correctly describes $\nabla \cdot \mathbf{u}$. This is very close to the prediction of DL, barring the small difference in the coefficient on the $\nabla \cdot \mathbf{u}/|\dot{\gamma}|$ term. As such, only the result for DL is shown (the oCIDR result is shown in the Supplemental Material [44]).

The results in Fig. 11 show that the prediction of IMUIR already gives a close match to the observed data, something that isn't apparent from Figs. 5(a) and 5(d). The results of CMUIR and iCIDR [Figs. 11(a) and 11(b)] are similar. The majority of points appear to fall close to the black line (denoting $|\sigma|_{\text{model}} = |\sigma|_{\text{DEM}}$); however, points drop below the line as $|\sigma|_{\text{DEM}}$ increases. This difference is more notable for CMUIR and likely arises due to both models incorporating an inverted $\phi(I)$ relationship ($\Psi(\phi)$). The deviation suggests that $\Psi(\phi)$ produces a value generally larger than I, which means for iCIDR $I/\phi(I) < 1$ and for CMUIR $P_{\text{eqb}} < P$ and hence $|\sigma|_{\text{model}} < |\sigma|_{\text{DEM}}$.

Despite this general trend, there are a few points where $|\sigma|_{model} \gg |\sigma|_{DEM}$, as seen in the inserts in Figs. 11(a) and 11(b). These points are associated with dense regions of flow wherein $\phi \to \phi_s$. Given the form of $\phi(I)$, and CMUIR and iCIDR both incorporating a dependence on $1/\Psi(\phi)$, as ϕ approaches ϕ_s, $|\sigma|_{model}$ approaches infinity. Thus while CMUIR and iCIDR produce reasonable predictions for $|\sigma|$, these predictions are poorer than that of IMUIR particularly in dense regions.

While CMUIR and iCIDR both perform significantly worse than IMUIR, DL [Fig. 11(c)] closely matches the simulations results (as does oCIDR). This model modifies IMUIR through the addition of a dilatancy term $\nabla \cdot \mathbf{u}/|\dot{\gamma}|$. The magnitude of this dilatancy term is generally small, and hence the differences between the predictions of DL and IMUIR are also small. Thus DL (and oCIDR) give a good match to $|\sigma|$. However, the expression $|\dot{\gamma}|K(\phi - \phi(I))$ fails to fully capture $\nabla \cdot \mathbf{u}$ (as shown in Fig. 10), and therefore it's unclear how well Eq. (15) would perform in practice.

3. Potential improvements

The models examined all capture some features of the simulated granular flows, but cannot account for all features. IMUIR and DL describe stress well, but not $\nabla \cdot \mathbf{u}$. Conversely, CMUIR and iCIDR describe $\nabla \cdot \mathbf{u}$ well, but do not describe stress well. Thus, the question is, are there any changes that could be made to improve the models? In this section we focus on CMUIR, looking at improving the result obtained when using the model to integrate the mass continuity. This model previously gave the best prediction for $\nabla \cdot \mathbf{u}$ and ϕ. The model also offers an immediate way of adjusting its prediction, by varying the parameter μ_b.

Figure 12 shows the prediction of CMUIR using different μ_b values. When a low value is used the model's prediction of the peak in ϕ (at $z/d_m \approx 15$) improves with the maximum ϕ closer to the true maximum. The peak is, however, shifted to the left (i.e., greater z). Figure 12 shows that by lowering μ_b, the prediction of CMUIR is improved, at least over the μ_b range considered. Particular improvement is seen for the vertical chute with hemicylindrical inserts, wherein the ϕ range examined is further from ϕ_s. A similar result is achieved using DL with a high K value (as shown in the supplemental material [44]). However, Fig. 9 suggests that using a low μ_b will worsen the prediction for $\nabla \cdot \mathbf{u}$ where $\nabla \cdot \mathbf{u}_{DEM}$ is very high or low. While Fig. 12 shows some improvement is possible, this is still insufficient. Heyman *et al.* [22] suggested μ_b is a function of ϕ. While it's possible that further improvements could be made by refining μ_b we were unable to derive a function $\mu_b(\phi)$ that would improve the results beyond what was achieved using a low μ_b value.

Next, we examine the definition of P_{eqb}. In Fig. 11 the use of P_{eqb} based on $\phi(I)$ to predict $|\sigma|$ gives poor results, and it may be causing similar issues with modeling $\nabla \cdot \mathbf{u}$ and ϕ. Thus, rather defining P_{eqb} using $\phi(I)$, we instead invert Eq. (11a) to get

$$P_{eqb} = |\sigma|/\mu(\phi). \tag{19}$$

Equation (19) is then used to integrate the mass continuity equation (6). The result of this integration is shown in Fig. 13, again using a range of μ_b values.

Figure 13 shows that the predictions of CMUIR are improved by using Eq. (19), with the best results achieved for $\mu_b \approx 1$. For the vertical chute with hemicylindrical inserts geometry [Figs. 13(a) and 13(b)], the improvement is similar to that achieved using a low μ_b with the standard CMUIR [hereafter we refer to CMUIR using Eq. (19) as CMUIRS]. For CMUIRS, we see that as the flow approaches the insert, the decrease in ϕ and $\nabla \cdot \mathbf{u}$ are captured quite well (something that is also seen in Fig. 12). However, the subsequent increase in ϕ and $\nabla \cdot \mathbf{u}$ as z decreases further are captured by the CMUIRS model significantly better than it was by the CMUIR model (Fig. 12).

The improvement for the chute with wedge inserts geometry [Figs. 13(c) and 13(d)], is even more significant. The minimum ϕ and $\nabla \cdot \mathbf{u}$ are both well captured, and the spike in ϕ and $\nabla \cdot \mathbf{u}$ are well defined, something CMUIR could not capture, even when μ_b was low. CMUIR's inability to capture this spike is likely due to $\psi(\phi) \to \infty$ as $\phi \to \phi_s$, which does not occur with $\mu(\phi)$ or Eq. (19). Regardless, Fig. 13 demonstrates how, by using CMUIRS, we can improve on the prediction of CMUIR, particularly for behavior in dense regions (though still in regions which would
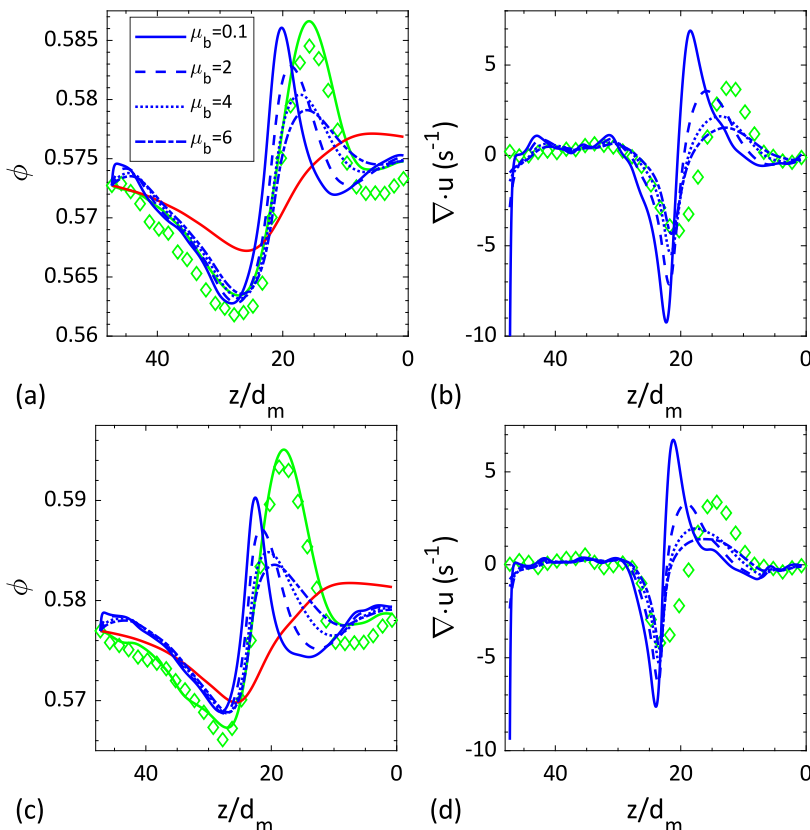
FIG. 12. Integration of the mass continuity to obtain ϕ in vertical chute with hemicylindrical (a) and wedge (c) inserts, using CMUIR. Panels (b) and (d) show the corresponding $\nabla \cdot \mathbf{u}$. Colors are as in Fig. 10.

be considered local). Alongside this analysis we also directly compared $\nabla \cdot \mathbf{u}_{\mathrm{DEM}}$ with $\nabla \cdot \mathbf{u}_{\mathrm{model}}$ for CMUIRS, finding that while predictions were not notably better than CMUIR when $|\nabla \cdot \mathbf{u}_{\mathrm{model}}|$ was large, they were somewhat improved when $\nabla \cdot \mathbf{u}_{\mathrm{DEM}}$ was close to 0 (see the Supplemental Material [44]). This is likely why CMUIR predicts an immediate jump in ϕ (in Fig. 10) where CMUIRS does not.

Using Eq. (19) demonstrates the improvements that can be made through modifying P_{eqb}. However, by removing the $\phi(I)$ equation, the set of equations is incomplete and the model is not closed. An additional relationship must be introduced to close the system. We considered introducing $|\sigma| = \mu(I)P$ from IMUIR to close the system, as Fig. 11 demonstrates IMUIR holds fairly well, but found the predictions of $\mu(I)$ and $\mu(\phi)$ were too similar and so unable to account for the difference between P and P_{eqb} obtained with Eq. (19). Other possibilities include deriving a new, more accurate, formula for P_{eqb} whilst maintaining Eq. (11a), or finding another way to define P. For example, Sun and Sundaresan [51] define local pressure from the fabric tensor and coordination number. Introducing these additional variables requires additional equations and so increases the complexity of the model. However, a modification like this may be necessary to allow CMUIR to accurately describe behavior in complex systems.

While not shown, it is possible to make similar modifications to DL, replacing $\phi(I)$ in Eq. (10b) with $\phi(\mu)$, and so introducing a dependence on stress into the definition of $\nabla \cdot \mathbf{u}$. The relevant figure is provided in the Supplemental Material [44] and the resulting improvements are similar, though not as significant, as those achieved with CMUIRS.
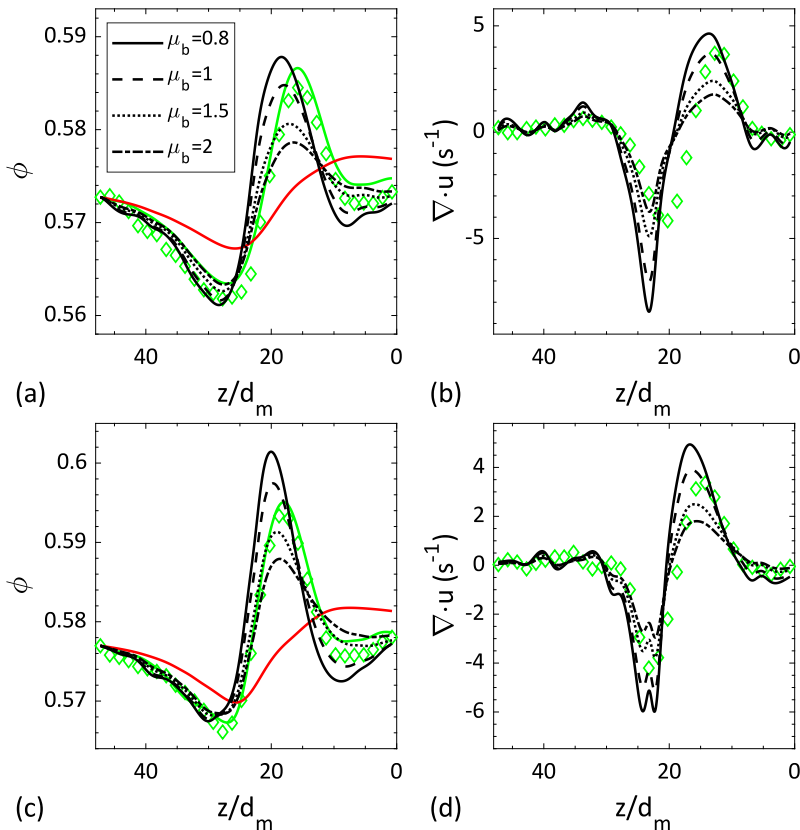
FIG. 13. Integration of mass continuity to obtain ϕ in vertical chute with hemicylindrical (a) and wedge (c) inserts, using CMUIRS. Panels (b) and (d) show the corresponding $\nabla \cdot \mathbf{u}$. Colors are as in Fig. 10, with black denoting CMUIRS.

The compressible models discussed all describe $\nabla \cdot \mathbf{u}$ as an approach to an equilibrium condition. This equilibrium is defined as the conditions at steady isochoric flow. For example, in CMUIR this equilibrium is defined (via P_{eqb}) through the $\phi(I)$ relationship that was derived in steady isochoric flow geometries. The results in Figs. 12 and 13 show that CMUIR can be improved by replacing the $\phi(I)$ relationship with the $\phi(\mu)$ relationship, which has also been recovered in steady isochoric flows and is valid over a wider range of conditions. However, it remains unclear how the equilibrium condition in nonisochoric and/or transient flows should be defined. Future work should consider whether other properties and/or relationships are needed to define equilibrium.

B. Nonlocal model analysis

The compressible models discussed to this point are all local models. The use of the $\phi(I)$ and $\mu(I)$ relations (which cannot describe any nonlocal effects and do not hold when $\phi > \phi_s$ or $\mu < \mu_s$) inherently restricts these models to local flows, even if we just consider the formulations for $\nabla \cdot \mathbf{u}$. Nonlocal models have been developed which introduce new variables and additional conservation equations [3,4,11]. However, most of these models were not developed for nonisochoric compressible flows, and maintain the assumption $\nabla \cdot \mathbf{u} = 0$. The need to account for nonlocality alongside dilatancy is apparent from Fig. 2, where deviations from $\phi(\mu)$ in nonisochoric systems occur most clearly in dense, low-shear, regions of flow where nonlocal effects are likely significant.
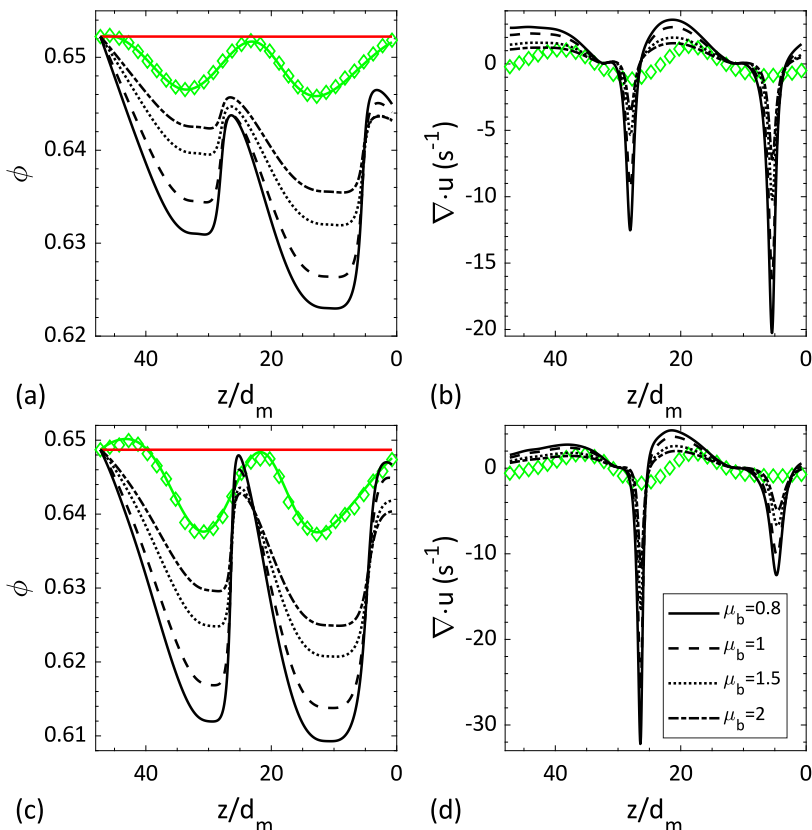
FIG. 14. Integration of mass continuity to obtain ϕ along centerline of vertical chute with hemicylindrical (a) and wedge (c) inserts, using CMUIRS. Panels (b) and (d) show the corresponding $\nabla \cdot \mathbf{u}$. Colors are as in Fig. 13.

In the prior section we proposed the CMUIRS model, in which $\phi(\mu)$ is used in place of $\phi(I)$. Thus CMUIRS could potentially be valid in dense regions of flow. We test this model in dense regions by taking the centerline of the two chute with inserts geometries ($x = 25d_m$) and again integrating the mass continuity equation, with the results shown in Fig. 14. These results show that in dense, nonlocal regions, CMUIRS is not able to capture the observed packing response. The CMUIRS model produces a much lower packing than is observed in the DEM simulations. This discrepancy appears to arise because when $|\sigma|$ is close to 0, $\nabla \cdot \mathbf{u}_{\mathrm{model}} \to \infty$ and hence CMUIRS cannot describe ϕ. This observation may indicate that nonlocality is manifesting both in the stress response, and in the velocity divergence, though further work would be needed to confirm this hypothesis.

Additionally, as discussed in the Sec. IV (and shown in Fig. 7), in dense regions of nonisochoric flows the alignment criterion [Eq. (5)] breaks down. Dilatancy results in a more complex response in these regions, which may be associated with nonlocality. There is at least one nonlocal model which uses a nonlocal form of the alignment criterion [52]. In this model, the orientation of the stress tensor is determined by the deviatoric strain rate but is modified by the deviatoric strain rate in the surrounding region using a diffusive term, i.e., $\nabla^2 \mathbf{D}'$. Such an approach appears promising and may be consistent with our data, however we were unable to confirm improved alignment with this approach.

It is clear from the results presented in this paper that, when describing nonisochoric flows, a model which accounts for both nonlocality and compressibility, and specifically their interaction, is necessary. The development of any such model is challenging, but remains a crucial area for further research.

VI. CONCLUSION

We have examined various compressible local continuum models in nonisochoric flows. The predicted velocity divergence and stress for these models was significantly different from the discrete simulation results. However, when applied to solve for the packing fraction by integrating the mass continuity equation, all of the models tested were able to capture key features of the flow. This included correctly predicting regions where packing fraction would increase or decrease in value. We demonstrate that the prediction of the CMUIR compressible model may be further improved by redefining how the equilibrium pressure is defined. While the modification made is impractical for general use, it suggests a direction for how this model might potentially be refined to improve the predictions in the future.

Despite the successes of these different local continuum models, it is unclear whether they could be extended into dense, potentially nonlocal, flow regions. We have examined the alignment criterion, showing that while it holds in these regions, provided flow is isochoric, it does not hold in these regions for nonisochoric flows. The observed failure of the alignment criterion in these regions complicates any nonlocal modification, particularly because this failure is evidently linked to the nonisochoric flows being compressible.

ACKNOWLEDGMENTS

[1] F. da Cruz, S. Emam, M. Prochnow, J.-N. Roux, and F. Chevoir, Rheophysics of dense granular materials: Discrete simulation of plane shear flows, Phys. Rev. E **72**, 021309 (2005).

[2] P. Jop, Y. Forterre, and O. Pouliquen, A constitutive law for dense granular flows, Nature (London) **441**, 727 (2006).

[3] I. S. Aranson and L. S. Tsimring, Continuum theory of partially fluidized granular flows, Phys. Rev. E **65**, 061303 (2002).

[4] M. Bouzid, A. Izzet, M. Trulsson, E. Clément, P. Claudin, and B. Andreotti, Non-local rheology in dense granular flows, Eur. Phys. J. E **38**, 125 (2015).

[5] D. L. Henann and K. Kamrin, A predictive, size-dependent continuum model for dense granular flows, Proc. Natl. Acad. Sci. USA **110**, 6730 (2013).

[6] P. V. Dsouza and P. R. Nott, Dilatancy-driven secondary flows in dense granular materials, J. Fluid Mech. **914**, A36 (2021).

[7] K. P. Krishnaraj and P. R. Nott, A dilation-driven vortex flow in sheared granular materials explains a rheometric anomaly, Nat. Commun. **7**, 10630 (2016).

[8] J. A. Robinson, D. J. Holland, and L. Fullard, Granular packing in complex flow geometries, Phys. Rev. Fluids **7**, 074304 (2022).

[9] S. Kim and K. Kamrin, Power-Law Scaling in Granular Rheology across Flow Geometries, Phys. Rev. Lett. **125**, 088002 (2020).

[10] G. Koval, J.-N. Roux, A. Corfdir, and F. Chevoir, Annular shear of cohesionless granular materials: From the inertial to quasistatic regime, Phys. Rev. E **79**, 021306 (2009).

[11] K. Kamrin and G. Koval, Nonlocal Constitutive Relation for Steady Granular Flow, Phys. Rev. Lett. **108**, 178301 (2012).

[12] T. S. Komatsu, S. Inagaki, N. Nakagawa, and S. Nasuno, Creep Motion in a Granular Pile Exhibiting Steady Surface Flow, Phys. Rev. Lett. **86**, 1757 (2001).

[13] P. Y. Lagrée, L. Staron, and S. Popinet, The granular column collapse as a continuum: Validity of a two-dimensional Navier-Stokes model with a $\mu(I)$-rheology, J. Fluid Mech. **686**, 378 (2011).

[14] L. Staron, P. Y. Lagrée, and S. Popinet, Continuum simulation of the discharge of the granular silo, Eur. Phys. J. E **37**, 5 (2014).

[15] C. Venier, L. Binda, D. Ramajo, S. Márquez Damián, I. Ippolito, and N. Nigro, The performance of the $\mu(I)$-rheology model on flat bottom silos discharge, EPJ Web Conf. **249**, 03032 (2021).

[16] L. Fullard, D. J. Holland, P. Galvosas, C. Davies, P.-Y. Lagrée, and S. Popinet, Quantifying silo flow using MRI velocimetry for testing granular flow models, Phys. Rev. Fluids **4**, 074302 (2019).

[17] T. Barker, D. G. Schaeffer, P. Bohorquez, and J. M. N. T. Gray, Well-posed and ill-posed behaviour of the $\mu(I)$-rheology for granular flow, J. Fluid Mech. **779**, 794 (2015).

[18] T. Barker and J. M. N. T. Gray, Partial regularisation of the incompressible $\mu(I)$-rheology for granular flow, J. Fluid Mech. **828**, 5 (2017).

[19] N. Martin, I. R. Ionescu, A. Mangeney, F. Bouchut, and M. Farin, Continuum viscoplastic simulation of a granular column collapse on large slopes: $\mu(I)$ rheology and lateral wall effects, Phys. Fluids **29**, 013301 (2017).

[20] T. Barker, M. Rauter, E. S. F. Maguire, C. G. Johnson, and J. M. N. T. Gray, Coupling rheology and segregation in granular flows, J. Fluid Mech. **909**, A22 (2020).

[21] T. Barker, D. G. Schaeffer, M. Shearer, and J. M. N. T. Gray, Well-posed continuum equations for granular flow with compressibility and $\mu(I)$-rheology, Proc. R. Soc. A **473**, 20160846 (2017).

[22] J. Heyman, R. Delannay, H. Tabuteau, and A. Valance, Compressibility regularizes the $\mu(I)$ rheology for dense granular flows, J. Fluid Mech. **830**, 553 (2017).

[23] B. Andreotti, Y. Forterre, and O. Pouliquen, *Granular Media: Between Fluid and Solid* (Cambridge University Press, New York, 2013).

[24] F. Bouchut, E. D. Fernández-Nieto, E. H. Koné, A. Mangeney, and G. Narbona-Reina, Dilatancy in dry granular flows with a compressible $\mu(I)$ rheology, J. Comput. Phys. **429**, 110013 (2021).

[25] D. G. Schaeffer, T. Barker, D. Tsuji, P. Gremaud, M. Shearer, and J. M. N. T. Gray, Constitutive relations for compressible granular flow in the inertial regime, J. Fluid Mech. **874**, 926 (2019).

[26] D. Gidaspow and M. Driscoll, Porosity and pressure waves in a fluidized bed of FCC particles, Ind. Eng. Chem. Res. **48**, 2422 (2009).

[27] J. van der Schaaf, J. C. Schouten, and C. M. van den Bleek, Origin, propagation and attenuation of pressure waves in gas-solid fluidized beds, Powder Technol. **95**, 220 (1998).

[28] S. Chialvo and S. Sundaresan, A modified kinetic theory for frictional granular flows in dense and dilute regimes, Phys. Fluids **25**, 070603 (2013).

[29] P. Jop, Y. Forterre, and O. Pouliquen, Crucial role of sidewalls in granular surface flows: Consequences for the rheology, J. Fluid Mech. **541**, 167 (2005).

[30] GDR MiDi (Groupement de Recherche Milieux Divisés), On dense granular flows, Eur. Phys. J. E **14**, 341 (2004).

[31] L. A. Fullard, E. C. P. Breard, C. E. Davies, A. J. R. Godfrey, M. Fukuoka, A. Wade, J. Dufek, and G. Lube, The dynamics of granular flow from a silo with two symmetric openings, Proc. R. Soc. A **475**, 20180462 (2019).

[32] T. Hatano, Power-law friction in closely packed granular materials, Phys. Rev. E **75**, 060301(R) (2007).

[33] T. Barker, C. Zhu, and J. Sun, Exact solutions for steady granular flow in vertical chutes and pipes, J. Fluid Mech. **930**, A21 (2021).

[34] M. Pailha and O. Pouliquen, A two-phase flow description of the initiation of underwater granular avalanches, J. Fluid Mech. **633**, 115 (2009).

[35] S. Roux and F. Radjai, Texture-dependent rigid-plastic behavior, in *Physics of Dry Granular Media*, edited by H. J. Herrmann, J. P. Hovi, and S. Luding (Springer Netherlands, Dordrecht, 1998), pp. 229–236.

[36] H. Shi, P. Dong, X. Yu, and Y. Zhou, A theoretical formulation of dilatation/contraction for continuum modelling of granular flows, J. Fluid Mech. **916**, A56 (2021).

[37] F. Bouchut, E. D. Fernández-Nieto, A. Mangeney, and G. Narbona-Reina, A two-phase two-layer model for fluidized granular flows with dilatancy effects, J. Fluid Mech. **801**, 166 (2016).

[38] C. Wang, Y. Wang, C. Peng, and X. Meng, Dilatancy and compaction effects on the submerged granular column collapse, Phys. Fluids **29**, 103307 (2017).

[39] X. Meng and Y. Wang, Modeling dynamic flows of grain-fluid mixtures by coupling the mixture theory with a dilatancy law, Acta Mech. **229**, 2521 (2018).

[40] M. Trulsson, M. Bouzid, P. Claudin, and B. Andreotti, Dynamic compressibility of dense granular shear flows, EPL (Europhys. Lett.) **103**, 38002 (2013).

[41] J. S. Fannon, I. R. Moyles, and A. C. Fowler, Application of the compressible i-dependent rheology to chute and shear flow instabilities, J. Fluid Mech. **864**, 1026 (2019).

[42] C. Kloss, C. Goniva, A. Hager, S. Amberger, and S. Pirker, Models, algorithms and validation for opensource DEM and CFD-DEM, Prog. Comput. Fluid Dyn. **12**, 140 (2012).

[43] Q. Zhang and K. Kamrin, A Microscopic Description of the Granular Fluidity Field in Nonlocal Flow Modeling, Phys. Rev. Lett. **118**, 058001 (2017).

[44] See Supplemental Material at http://link.aps.org/supplemental/10.1103/PhysRevFluids.8.014304 for (i) additional detail on DEM setup, (ii) ϕ vs I, μI, and ϕ vs μ in chute with wedge inserts, (iii) wall velocities for split bottom shear cell, (iv) additional figures of integration of mass continuity in chute with inserts geometries, and (v) prediction of $|\sigma|$ using the oCIDR model.

[45] I. Goldhirsch, Stress, stress asymmetry and couple stress: From discrete particles to continuous fields, Granular Matter **12**, 239 (2010).

[46] D. R. Tunuguntla, A. R. Thornton, and T. Weinhart, From discrete elements to continuum fields: Extension to bidisperse systems, Comput. Particle Mech. **3**, 349 (2016).

[47] T. Weinhart, C. Labra, S. Luding, and J. Y. Ooi, Influence of coarse-graining parameters on the analysis of DEM simulations of silo flow, Powder Technol. **293**, 138 (2016).

[48] J. A. Robinson, D. J. Holland, and L. Fullard, Examination of the microscopic definition for granular fluidity, Phys. Rev. Fluids **6**, 044302 (2021).

[49] S. Volpato, R. Artoni, and A. C. Santomaso, Numerical study on the behavior of funnel flow silos with and without inserts through a continuum hydrodynamic approach, Chem. Eng. Res. Design **92**, 256 (2014).

[50] Y. Forterre and O. Pouliquen, Flows of dense granular media, Annu. Rev. Fluid Mech. **40**, 1 (2008).

[51] J. I. N. Sun and S. Sundaresan, A constitutive model with microstructure evolution for flow of rate-independent granular materials, J. Fluid Mech. **682**, 590 (2011).

[52] P. V. Dsouza and P. R. Nott, A non-local constitutive model for slow granular flow that incorporates dilatancy, J. Fluid Mech. **888**, R3 (2020).

[53] See, https://www.nesi.org.nz.